

## Article

# Microstructure and Corrosion Behavior of Ti-Nb Coatings on NiTi Substrate Fabricated by Laser Cladding

Jie Hu <sup>1</sup>, Yaojia Ren <sup>1</sup>, Qianli Huang <sup>1</sup>, Hao He <sup>2,\*</sup>, Luxin Liang <sup>1</sup>, Jingbo Liu <sup>1</sup>, Ruidi Li <sup>1</sup> and Hong Wu <sup>1,\*</sup>

<sup>1</sup> State Key Laboratory of Powder Metallurgy, Central South University, Changsha 410083, China; jiehuu@csu.edu.cn (J.H.); 125ren@163.com (Y.R.); hq11990@163.com (Q.H.); Liang\_luxin@163.com (L.L.); jingbo-liu@csu.edu.cn (J.L.); liruidi@csu.edu.cn (R.L.)

<sup>2</sup> Department of Vascular Surgery, Second Xiangya Hospital, Central South University, Changsha 410011, China

\* Correspondence: jimmyhehao@gmail.com (H.H.); hwucsu@csu.edu.cn (H.W.)

**Abstract:** Ti-23Nb (at.%) coatings on an NiTi alloy with metallurgical bonding were prepared by laser cladding (LC) technology using Ti-Nb mixture powders. The effects of laser processing parameters on the microstructure and mechanical properties of the coatings were systematically investigated and the corrosion resistance of the coatings was assessed. The coatings were composed of TiNb, (Ti, Nb)<sub>2</sub>Ni, and β-Nb phases. The coatings increased the hardness of the NiTi alloy by a combined strengthening effect of the eutectics and fine microstructure. The corrosion resistance of the coated part was improved. The coatings with great corrosion resistance could keep the coated parts inert in an aggressive environment, and effectively restrain the release of toxic Ni ions, which means that the Ti-Nb alloy coatings are likely to be used as a biomaterial for medical applications.

**Keywords:** laser cladding; Ti-Nb alloy coating; NiTi(Nb) phase; microstructure; corrosion resistance



**Citation:** Hu, J.; Ren, Y.; Huang, Q.; He, H.; Liang, L.; Liu, J.; Li, R.; Wu, H. Microstructure and Corrosion Behavior of Ti-Nb Coatings on NiTi Substrate Fabricated by Laser Cladding. *Coatings* **2021**, *11*, 597. <https://doi.org/10.3390/coatings11050597>

Academic Editors: Cecilia Bartuli and Ingrid Milošev

Received: 29 March 2021

Accepted: 12 May 2021

Published: 19 May 2021

**Publisher's Note:** MDPI stays neutral with regard to jurisdictional claims in published maps and institutional affiliations.



**Copyright:** © 2021 by the authors. Licensee MDPI, Basel, Switzerland. This article is an open access article distributed under the terms and conditions of the Creative Commons Attribution (CC BY) license (<https://creativecommons.org/licenses/by/4.0/>).

## 1. Introduction

Titanium alloys are widely employed as biomaterials because they offer great functionality, biocompatibility, great corrosion resistance, and mechanical properties [1–4]. Among them, NiTi shape memory alloys (SMAs) have been extensively assessed in terms of superelasticity (SE) [5–7], usage for orthodontic arch wire, self-expanding stent, and embracing fixator, etc. [8–10].

The applications of the NiTi alloys are still limited, owing to the damaged surface of the alloys, and further leading to release of toxic Ni ions [11,12]. The release of toxic ions has increasingly attracted concerns, because if the toxic ion content in the human body environment exceeded a certain threshold value  $0.2 \mu\text{g}\cdot\text{cm}^{-2}$ , it would cause toxic and allergic reactions and influence gene expression and cholesterol metabolism [13,14]. Besides, “Nickel cases” constantly appear, despite the fact that nickel recovery is very low in in vitro physiological studies or drops to undetectable levels in a physiological environment [15]. Therefore, preventing Ni ions releasing from biomaterials into the human body is compulsory for NiTi alloys to be successfully used for biomedical applications [16,17].

To prevent Ni ions release, an increasing number of studies started to focus on improving the corrosion resistance of titanium alloys via surface modification methods [18], while maintaining the mechanical properties of the substrate [19,20]. For example, the resistance to corrosion can be improved by laser surface melting, coating, and magnetron sputtering techniques. Sun et al. [21] reported the (Si, O, N)/(Ti, O, N)/Ti composite coating, which was fabricated by magnetron sputtering following plasma immersion ion implantation and deposition (PIIID), could promote corrosion resistance in the in vitro environment, and bioactivity of NiTi alloys. Compared to traditional methods, the laser cladding (LC) technique is becoming increasingly popular due to its low cost, high flexibility, and strong metallurgical bond with no risk of coating delamination [22,23]. Besides, the technique

is capable of producing fine microstructures with outstanding mechanical properties, including strength and fracture resistant [24–26]. Fallah et al. [27] reported that LC-built Ti-Nb alloys could restrain toxic V ions releasing from Ti6Al4V and steel substrates. Ti-Nb alloys have good biocompatibility and corrosion resistance [28–30], and are even expected to replace NiTi alloys in the field of biomedical applications [31–34]. Preparing Ti-Nb components through the conventional method is rather costly due to the high melting point of Nb. Instead, a possible alternative way to take advantage of the Ti-Nb alloy is to apply its coatings on the NiTi substrate, rather than producing the bulk of component in the Ti-Nb alloy, which could be more easily achieved and also cost effective.

In this work, Ti-Nb alloy coatings on the NiTi substrate were fabricated by the LC technique. We investigated the effects of LC processing parameters on the microstructure and mechanical properties of Ti-Nb alloy coatings on the substrate. Then, the corrosion resistance of the coatings and the NiTi alloy was compared. Laser cladding of Ti-Nb coatings has rarely been studied. Additionally, it is expected that the results from this study could facilitate further application of the NiTi alloy for long-term biomedical implantation.

## 2. Material and Methods

### 2.1. Materials and Preparation Process

Cold rolled NiTi alloy was used as the substrate and was cut into 100 mm × 100 mm × 8 mm plate. The chemical composition of the NiTi material consisted of 50.9 at.% Ni, 0.039% O, 0.030% C, and 0.003% N, balanced with Ti. Irregularly shaped Ti powders (purity ≥ 99.75 wt.%) and Nb powders (purity ≥ 99.36 wt.%) were blended in a mixer (Turbula T2F, Switzerland) for 9 h to achieve a uniform distribution. The proportion of Ti powder and Nb powder was 77 to 23 at.%. The average size of Nb particles ( $D_{50} = 70.5 \mu\text{m}$ ) were smaller than that of Ti ( $D_{50} = 83.1 \mu\text{m}$ ). The mixed powders were handled in a glove box with argon gas protection. To remove the oxide layer and contaminants on the outer surface of NiTi substrate, the plate was polished with SiC abrasive papers (400#, 800#, 1200# grit), then sequentially cleaned with acetone, de-ionized water, and anhydrous ethanol.

A MFSC-500 fiber laser system with a 2.0 mm spot diameter and 1.08  $\mu\text{m}$  wavelength was used for the cladding while the powders were coaxially fed into the laser spot, as illustrated in Figure 1a.

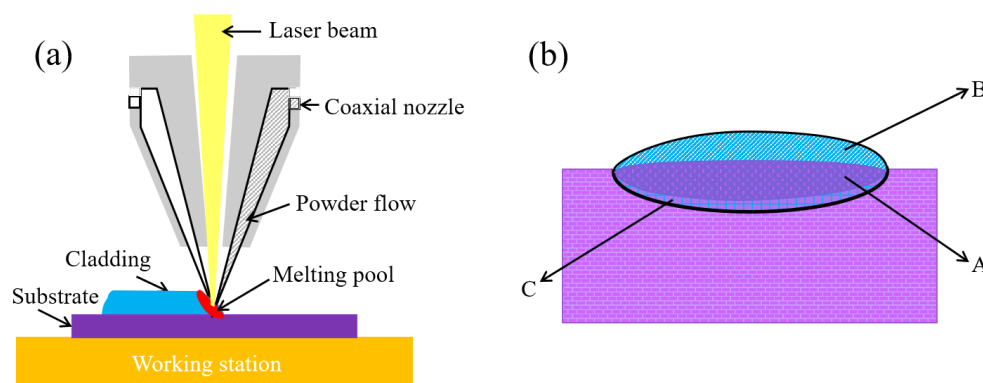


**Figure 1.** Schematic of the fundamental of laser cladding technique, (a) the experimental setup; (b) dilution in a bulk coating: A, a solution zone of substrate with coating; B, coating; C, heat affected zone (HAZ).

The substrate was partially melted and mixed with the cladded material, where three different zones can be observed on the cross-sectional view, i.e., solution zone of substrate with coating (A), coating material (B), and heat affected zone (HAZ) (C), as indicated in Figure 1b. To avoid absorption of oxygen and nitrogen into the molten pool during laser cladding process, the entire working cabin was shielded with the Argon. Further, the Argon with 25 L·min<sup>-1</sup> flow rate was used to convey powder mixture. The laser was scanned uni-directionally at a velocity between 1.6–3.6 mm·s<sup>-1</sup> and an overlap of 70%,

respectively. Table 1 summarizes the pulsed laser cladding processing parameters. In the work, the energy density ( $E$ ) was chosen to measure the unit of energy flow rate. The energy density  $E$  ( $\text{J}\cdot\text{mm}^{-2}$ ) shows:

$$E = \frac{P}{VD} \quad (1)$$

where  $P$  is the laser power (W),  $V$  is the laser scan speed ( $\text{mm}\cdot\text{s}^{-1}$ ), and  $D$  is the laser beam diameter (mm). To observe the structure morphology of the coatings, the cross-section was further ground with SiC abrasive papers and then polished with OPS reagent (grain size  $0.04\ \mu\text{m}$ ). Then, the specimens were chemically etched for about 15 s in a solution containing 10% HF, 15%  $\text{HNO}_3$ , and 75% deionize water to characterize the microstructure.

**Table 1.** Processing parameters of the pulsed laser cladding.

Samples	Laser Power (W)	Scanning Velocity ( $\text{mm}\cdot\text{s}^{-1}$ )	Beam Diameter (mm)	Overlap Ratio (%)	Energy Density ( $\text{J}\cdot\text{mm}^{-2}$ )
c1	350	1.6	2.0	70	109
c2	350	2.0	2.0	70	88
c3	350	2.6	2.0	70	67
c4	350	3.0	2.0	70	58
c5	350	3.6	2.0	70	49

## 2.2. Material Characterization

The particle size distributions of powders were analyzed by a laser particle size analysis meter (Mastersizer 3000, Malvern Panalytical, Malvern, UK). The CP-Ti powder had a  $D_{50} = 83\ \mu\text{m}$ . Nb powder had a  $D_{50} = 77\ \mu\text{m}$ . Phase composition was analyzed by X-ray diffraction (XRD, Advance D8, Bruker, Billerica, MA, USA) with a continuous scanning mode over a wide range of  $2\theta = 30^\circ \sim 90^\circ$  with a scanning rate of  $6^\circ/\text{min}$ , using a  $\text{Cu K}\alpha$  radiation source ( $\lambda = 1.54\ \text{\AA}$ ; 40 mA and 40 kV). Metallographic specimens were prepared by following the procedures mentioned above. The microstructures of the samples were characterized via optical microscopy (OM, DM2700P, Leica, Germany), scanning electron microscopy (SEM, FEI Quanta 250 FEG, Lausanne, Switzerland), and high-resolution scanning electron microscopy (HRSEM, Helios Nanolab G3 UC, FEI, Lausanne, Switzerland). Element distributions analysis was performed by energy dispersive spectroscopy (EDS, Aztec Energy X-max 80, Brentwood, NY, USA).

## 2.3. Nano-Indentation

The hardness and Young's modulus of the top surface of the laser tracks were measured by nano-indentation tester (NHT, CSM, Peseux, Switzerland) with loading 40 mN and loading rate  $1\ \text{mN}\cdot\text{s}^{-1}$ . The Vickers hardness variation with the depth of each cross-sectional coating was measured under a micro-indentation tester with 200 g load and 15 s dwelling time. Twenty areas were measured in each depth.

## 2.4. Electrochemical Corrosion Behavior

The electrochemical corrosion behavior of the Ti-Nb alloy coatings and bare NiTi alloy was assessed in a typical three-electrode cell containing simulated body fluid (SBF,  $\text{pH} = 7.4$ ) as the electrolyte at  $37 \pm 0.1\ ^\circ\text{C}$ , by using a PARSTAT-4000 (Princeton Applied Research, Oak Ridge, TN, USA) electrochemical station. The ion concentrations in SBF solution are shown in Supplementary Materials (Table S1). The corrosion cell consisted of a saturated calomel reference electrode, counter electrode (Pt), and the specimen as the working electrode. The working surface was  $7 \times 7\ \text{mm}^2$ . The OCP (open circuit potential) was performed for 60 min to reach a relatively stable level. The fluctuation of OCP is less than 5 mV every 10 min. The polarization tests were carried out at a scanning rate of  $1\ \text{mV}\cdot\text{s}^{-1}$ . Corrosion potential ( $E_{\text{corr}}$ ) and current density ( $I_{\text{corr}}$ ) could be worked out from

the polarization curves by Tafel analysis. Each test was repeated three times to obtain an averaged result.

### 3. Results and Discussion

#### 3.1. Microstructure Characteristics

As shown in Figure 2a,b, the irregularly shaped Ti-23Nb mixed powders show a uniform distribution. The bright area represents Nb powder in Figure 2a. The blue area shows Nb powder in Figure 2b. Figure 2c reveals that the NiTi alloy mainly shows the B2 phase (Pm-3 m) with diffraction peaks of (110) and (211). Ti and Nb phases in the mixed powder show the  $\alpha$ -Ti phase (hcp structure) and bcc structural  $\beta$ -Nb phase (bcc structure), respectively.

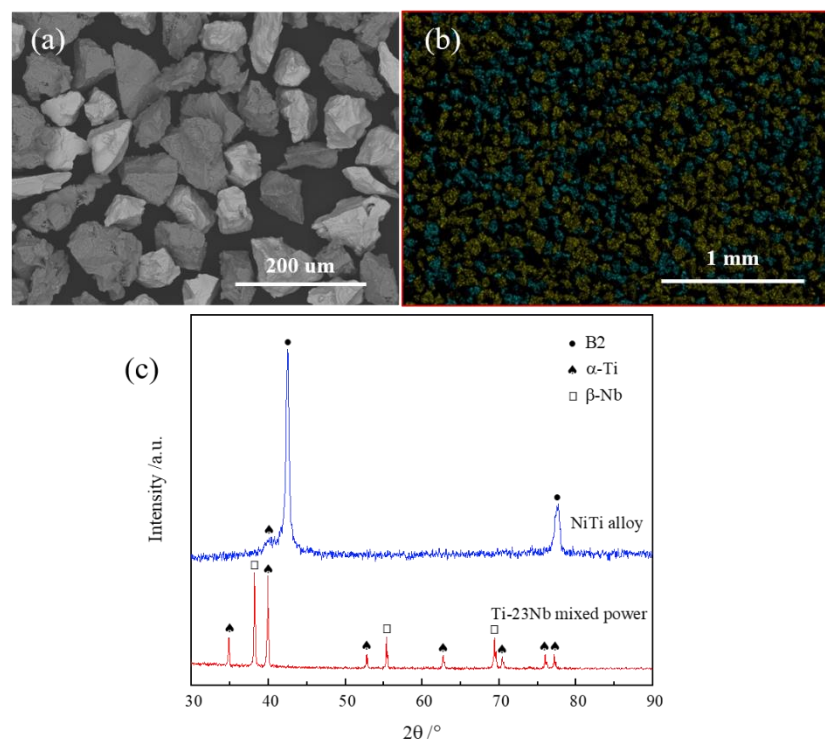


**Figure 2.** SEM micrographs of the mixture of pure Ti and Nb powders, showing (a) morphology and (b) EDS mapping results at a low magnification; (c) XRD patterns of the powder mixture and NiTi alloy substrate, respectively.

OM images of the cross-section of Ti-Nb alloy coatings are shown in Figure 3. OM images of Ti-Nb coatings obtained under various cladding conditions showed similar morphology, which consisted of the molten pool, the HAZ, and the welding line. Due to the heat impact during the cladding process, an area undergoing microstructural and property changes could be identified as HAZ, shown in the yellow area. HAZ generally has coarse cellular grain structures in the bright area up the welding line [35], which will be explained later. With the laser energy density decreasing from 109 to 58 J·mm<sup>-2</sup>, the width of the HAZ became narrower. The coatings with a thickness of about 600 μm bonded well with the substrate, but few unmolten particles can still be spotted in the coated layer. The gas pores were trapped and microcracks were also observed in the HAZ of the coating c1, as shown in Figure 3d. The microcracks extended from the welding line to the surface of the coating. No cracks were formed in the other coatings. The formation of microcracks in the HAZ resulted from the stress concentration during the rapid melting and solidification and trapped pores. Besides, the grains are coarse and brittle in the HAZ [36], which easily lead to cracks, as shown in Figure 3d. The microcrack of the Ti-Nb alloy coating would cause premature failure in service, which hinders its further application in industry [37].

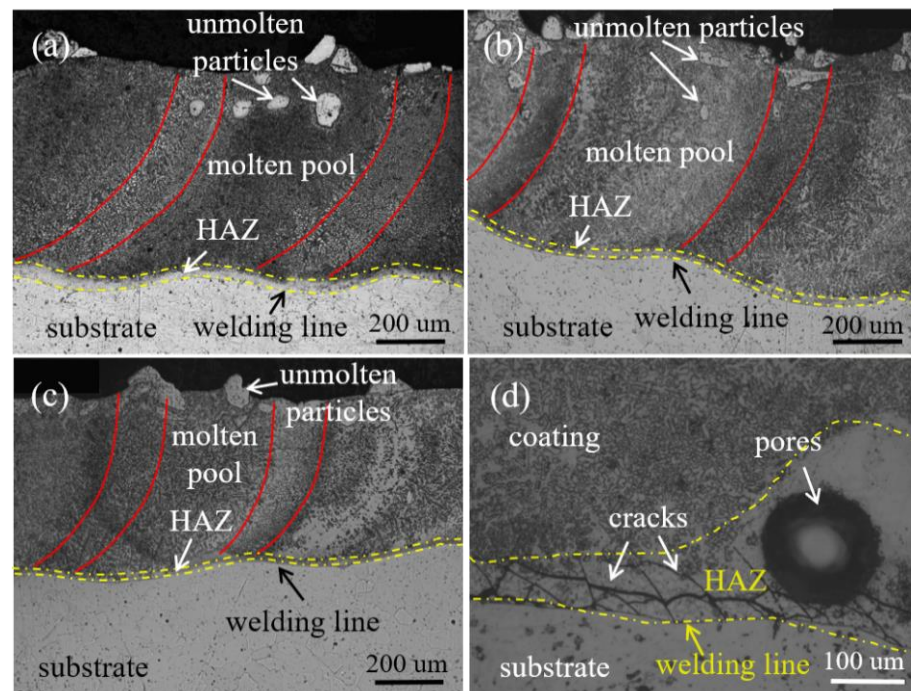


**Figure 3.** OM images observed in the cross-section of Ti-Nb alloy coatings at different energy densities respectively: (a)  $109 \text{ J}\cdot\text{mm}^{-2}$ ; (b)  $88 \text{ J}\cdot\text{mm}^{-2}$ ; (c)  $58 \text{ J}\cdot\text{mm}^{-2}$ ; and (d) showing pores and cracks in the c1 coating.

The microstructures of the Ti-Nb alloy coatings at different energy densities are shown in Figure 4. The mid-height areas of the coating are shown in Figure 4a,d,g. The primary phases are shown in equiaxed oval and dendrite structures. The primary phases were rapidly solidified due to the coarse interface between solid and liquid combining with large undercooling. Ti and Nb atoms can substitute each other in crystal lattice and form an infinite solid solution [38]. Because Ni atoms diffused from the substrate into the coating, the primary phases contained TiNb,  $(\text{Ti}, \text{Nb})_2\text{Ni}$ , and NiTi(Nb). When the temperature of the molten pool dropped, the residual liquid phase started to form eutectics which were uniformly and continuously distributed in the primary phase matrix. As the temperature continued to fall,  $\alpha$  phase precipitated from primary phases and eutectics. The  $\alpha'$  and  $\alpha''$  phases from the mother phase could be precipitated due to martensite transformation. The structures at the bottom of the coatings are similar under high energy density, different from that under low energy density, with the fine equiaxed dendrite shown in Figure 4b,e,h. Besides, the microstructures of the HAZ are different from that of the coatings, shown in Figure 4c,f,i. Cellular grains were formed in the HAZ, because of the positive temperature gradient between solid and liquid interface and the smaller subcooling degree of composition. The mesh eutectic structure was formed due to solute atoms segregating at grain boundaries in the heat affected zone, which showed lamellar-type and rod-like microstructures [38,39]. Such microstructures presented the NiTi(Nb) alloy microstructure, mainly consisting of primary phase NiTi(Nb) and eutectics of NiTi(Nb) and  $\beta$ -Nb [40,41]. The eutectic region of the coatings with a high energy density was continuous. The lower the energy density, the smaller the width of the eutectic area.

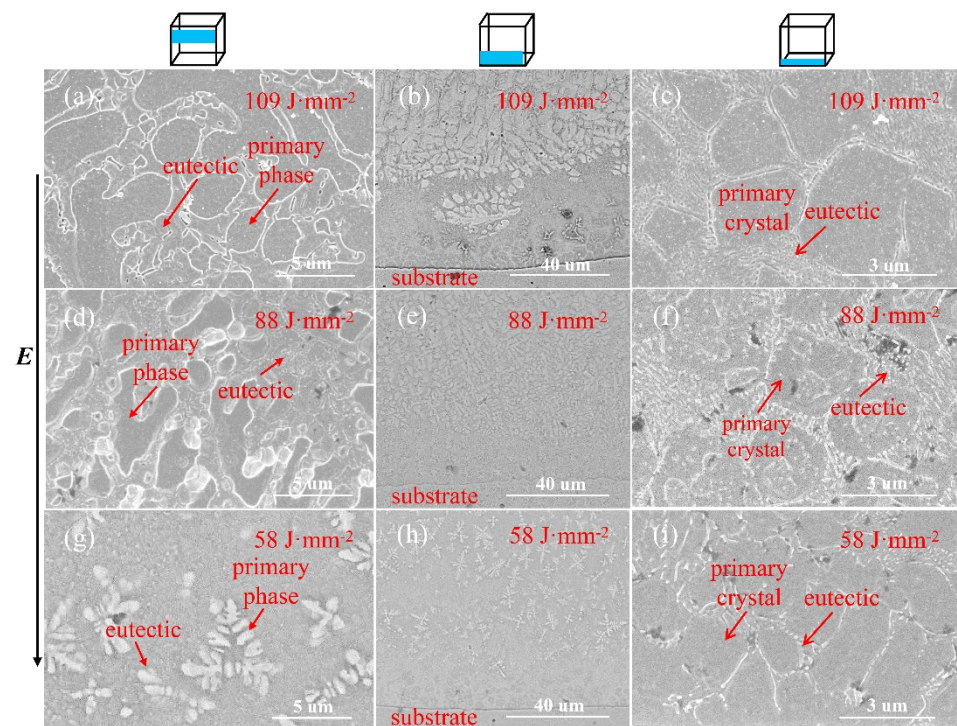


**Figure 4.** SEM morphologies of cross-sections of the Ti-Nb coatings: (a,d,g) the mid-height and (b,e,h) the bottom of the coatings under the energy densities of  $109 \text{ J}\cdot\text{mm}^{-2}$ ,  $88 \text{ J}\cdot\text{mm}^{-2}$ ,  $58 \text{ J}\cdot\text{mm}^{-2}$ ; (c,f,i) the HAZ of those coatings in high magnification, respectively.

As shown in Figure 4, with the decrease of energy density, i.e., the increase of scanning velocity, the grain size gradually became smaller correspondingly. There are fine equiaxed dendrites in the molten pool at low energy density, which is consistent with the results of Co-based coatings containing Nb prepared by plasma cladding [42]. There are coarse cellular dendrites at high energy density. The growth of dendrites and equiaxed grains can be influenced by the local composition and temperature gradient [43]. With the increase of scanning rate, the temperature gradient and undercooling degree in the molten pool increased, then the driving force for phase transformation and the solidification speed increased correspondingly. With the increase of undercooling, the critical nucleation radius decreased and the nucleation rate increased, resulting in the finer grain sizes of the cladding layer. The fine microstructure would lead to difference in mechanical properties [44]. In a certain range, finer grain structures are beneficial for improving the strength and toughness of materials. Besides, the laser processed surface with more Ti content may have better biocompatibility and corrosion resistance [45]. Therefore, performing the laser cladding at relatively lower energy density is likely to improve the biomedical properties of LC-built Ti-Nb coatings.

The elemental distribution in LC-built Ti-23Nb alloy coatings was examined by using an SEM equipped with EDS. As shown in Figure 5, the distribution of Ti and Nb in the coating was not homogeneous, similar phenomena reported in literature [46,47] as well. The bright phase was rich in Ti and Nb but in depletion of Ni, while Ni elements were enriched in the dark phases. Ni atoms diffused from the substrate into the coatings and the concentration of Ni gradually decreased from the substrate towards the coating surface. A few Nb atoms diffused into the HAZ due to heat effect. Zhao et al. [40,48] reported that low Nb content in NiTi(Nb) alloys could develop a wide hysteresis by pre-deformation. The biomedical application of the alloys could also be affected correspondingly. The solution zone between the coating and substrate results from the elemental dilution. Part of the substrate was melted and mixed into the melt pool with the help of hot flow movement and mutual diffusion of the elements, then rapidly solidified. In general, a small number of

percentages of the dilution rate is often desirable in depositing coating materials. However, it is difficult to achieve and the dilution rate values are typically in the range between 10% and 40% [49].

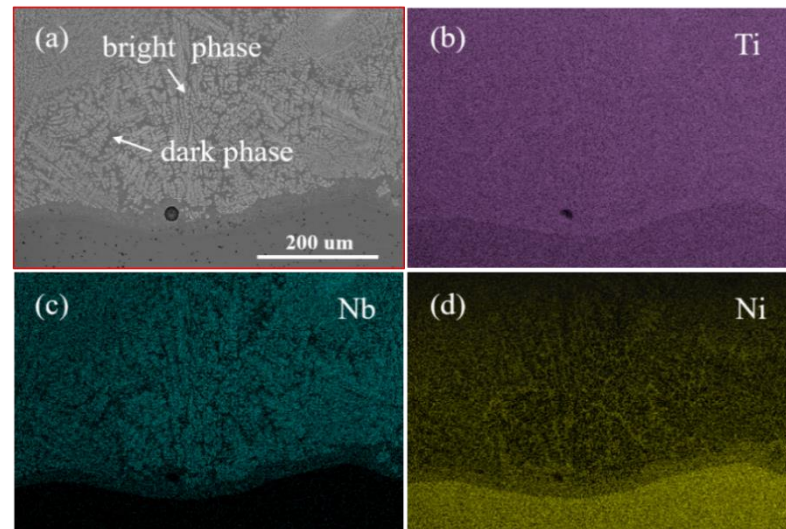


**Figure 5.** EDS mapping analysis results of the coating from the substrate to the coating, (a) showing SEM image with the bright phase and the dark phase; (b–d) showing different elemental distributions, respectively.

Figure 6 presents XRD patterns of the Ti-Nb alloy coatings. The results indicated that there were mainly the TiNb phase (bcc),  $(\text{Ti, Nb})_2\text{Ni}$  phase (fcc), and NiTi(Nb) phase (B19') in the coatings. With an decrease of the energy density, the volume of the  $\beta$ -Nb grains increases, and the NiTi(Nb) phase and  $(\text{Ti, Nb})_2\text{Ni}$  phase decreased remarkably. The Ti-Nb binary alloy is in the form of infinite solution  $\beta$  phase at high temperature. Metastable  $\beta$  phase was maintained to room temperature during rapid solidification. When the temperature lowered to 882 °C,  $\alpha$  phase precipitated from  $\beta$  phase, as shown at the peak at 40.17°. Besides, there was a high peak of the martensite  $\alpha''$  NiTi(Nb) phase in the diffraction pattern. The martensite  $\alpha''$  phase was formed from the mother phase under martensite transformation starting temperature ( $M_s$ ) [5]. In short, when energy density is lower, the LC-built Ti-Nb coatings can obtain more  $\beta$  TiNb phase and  $\beta$ -Nb phase which have low elastic modulus. Unmolten Nb particles are hard to eliminate at all times. Nb grains in an appropriate range of dimensions in the Ti-Nb alloy coating could strengthen alloy strength and toughness [41].

### 3.2. Micromechanical Analysis

As shown in Figure 7, the microhardness (H) and elastic modulus (E) of the NiTi alloy were 233.1 HV and 54.2 GPa, respectively. With an increase of the energy density, H and E of the coatings decreased. However, the H and E of various coatings were higher than those of the NiTi alloy. The E of the coating with the energy density of 88 J·mm<sup>-2</sup> was the lowest among the specimens. Figure 7b shows the maximum H over 1000 HV in the HAZ, which is rarely reported. This result is attributed to the existence of nanocrystalline eutectics. With the distance of the HAZ in the coatings, the hardness of the cross sections gradually decreased, owing to the depleted Ni atoms in the coatings.

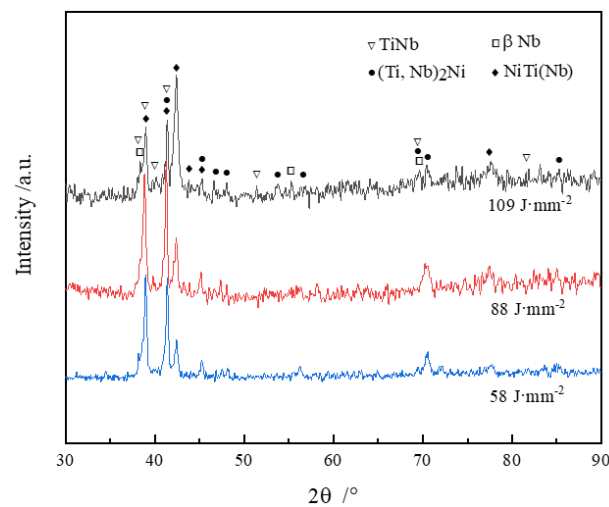


Figure 6. XRD patterns of the Ti-Nb alloy coatings with energy density from 109~58  $\text{J}\cdot\text{mm}^{-2}$ .

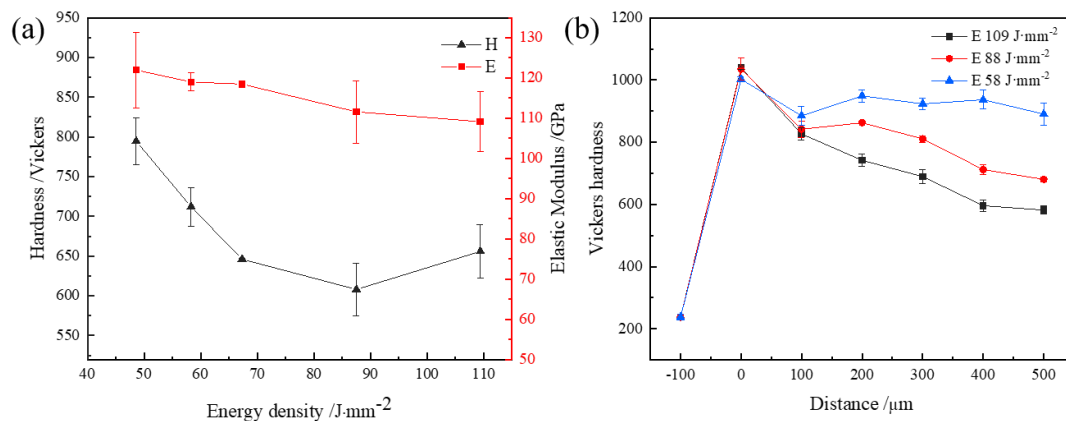


Figure 7. Mechanical properties of the Ti-Nb alloy coatings, (a) nano-indentations of the top surface; (b) the Vickers hardness of the cross section from the substrate to the coating. The distance at the HAZ is 0  $\mu\text{m}$ .

The mechanical properties of the Ti-Nb alloy relies on the microstructure of the molten pool, which is mainly affected by temperature and concentration gradients, and growth of grain [50]. The grain sizes were finer in the coatings obtained with lower energy density (Figure 4), while the values of H and E increased accordingly (Figure 7). Accordingly, the capability of materials resisting deformation at room temperature was improved. Apart from the fine microstructure, the specific atom-level bonding conditions in the coating were closely related to such difference in hardness. Bond order (Bo) of the d-d covalent bond between atoms was evaluated by Mulliken [51]. However, given the specific conditions of alloys, the bond order of each element is divided by its atomic weight to measure the relative strength of the bond [52]. With a higher ratio, the ratio of bond order to atomic weight is stronger, and the molecules are stabler. The ratio for Ti-M mainly depends on the alloying element, M. The variation trend of the bond order is similar between hcp and bcc Ti. Therefore, the ratio of Ti-Nb is larger than that of Ti-Ni. Therefore, the strength of the Ti-Nb alloys coatings is stronger than the bare Ti-Ni alloy.

The H of the cross-sectional coating c2 (the building direction in additive manufacturing) and the top surface (the scanning direction) is  $680.6 \pm 7.3$  HV and  $608.10 \pm 33.0$  HV, respectively. The difference demonstrates the mechanical anisotropy of the coating and the lower hardness at the top surface. In recent years, studies about mechanical properties of Ti-based alloys have been widely reported, as shown in Table 2. In contrast, the LC-built

Ti-Nb coatings own great mechanical properties, even bond metallurgically well with the NiTi alloy substrate, which could be used as biomedical appliances.

**Table 2.** Typical tensile tests and microhardness values of the Ni-Ti alloys, Ti-Nb alloys, and other Ti alloys.

Alloys	Preparation Methods	Tensile Strength (MPa)	Young's Modulus (GPa)	Microhardness (HV <sub>0.2</sub> )	Reference
Ni55Ti	Hot-rolling	-	-	220	[22]
NiTi	LC	320	21	~430	[53]
Ti30Nb	LC	-	-	850	[47]
Ti-35Nb	LC	-	-	700	[22]
Ti-23Nb	LC	-	109 ± 7	656 ± 34	This work
Ti-25Nb	SLM	748 ± 27	83.5 ± 0.8	264 ± 6	[54]
Ti-30Nb	Remelting	527	64.3	233.4	[13]
Ti-23Nb	SPS	-	-	455	[8]
Ti-25 Nb	SLM	923 ± 38	18.7 ± 1.4	297 ± 3	[55]
Ti-13Nb-13Zr	SLM	1020 ± 13	67	-	[56]

### 3.3. Electrochemical Corrosion Analysis

To investigate the corrosion resistance of the scanning direction of LC-built Ti-Nb alloy coatings in SBF solution, electrochemical tests were carried out. The bare NiTi alloy was used as the contrast group. The polarization curves of the samples are shown in Figure 8. The polarization behavior contains two sections: the oxidation of the electrode on the anode and the hydrogen evolution reaction on the cathode. The coatings exhibited stable passivation behavior due to a protective film formed, i.e., NbO, NbO<sub>2</sub>, Nb<sub>2</sub>O<sub>5</sub>, and TiO<sub>2</sub>, which had great corrosion resistance at high oxidation potential and could restrain further corrosion of the coatings [22].

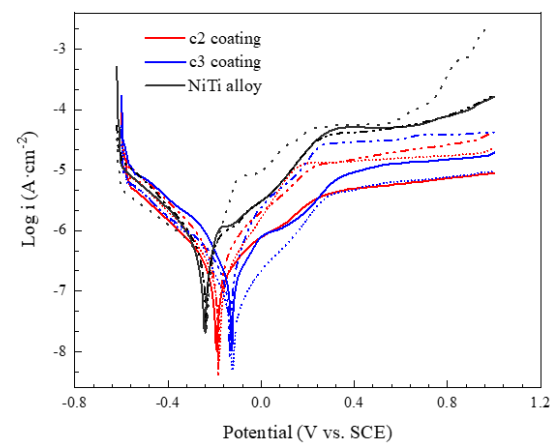


**Figure 8.** The potentiodynamic polarization curves for the Ti-Nb alloy coatings and bare NiTi alloy under immersion in SBF. The curves (line, dotted, dashed) in the same color are repetitions.

The average corrosion potential ( $E_{\text{corr}}$ ), corrosion current density ( $I_{\text{corr}}$ ), and polarization resistance ( $R_p$ ) of the samples in SBF solution were calculated from the polarization curves, respectively, as presented in Table 3. The  $E_{\text{corr}}$  can measure the difficulty in corrosion of materials. A higher  $E_{\text{corr}}$  indicates that the materials are harder to be corroded. The  $I_{\text{corr}}$  reflects the corrosion speed of materials. A higher  $I_{\text{corr}}$  indicates a faster corrosion rate [57,58]. The  $R_p$  is inversely proportional to the  $I_{\text{corr}}$ .  $R_p$  can also qualitatively judge the corrosion resistance of materials. A larger  $R_p$  exhibits a stronger corrosion resistance. Ti-Nb alloy coatings have higher  $E_{\text{corr}}$  than the NiTi alloy substrate, laser processed NiTi alloy, and Ti-13Nb-13Zr alloy. The  $I_{\text{corr}}$  of the Ti-Nb alloy coating was significantly lower than

that of the substrate, laser processed NiTi alloy, and Ti-13Nb-13Zr alloy. Besides, Ti-Nb alloy coatings possessed larger  $R_p$  than the NiTi alloy. Therefore, the LC-built Ti-Nb alloy coatings have better corrosion resistance than the NiTi alloy, laser processed NiTi alloy, and Ti-13Nb-13Zr alloy. The  $E_{corr}$  and  $I_{corr}$  values of the coating c3 were  $-0.128 \pm 0.005$  V and  $I_{corr}$  of  $163.7 \pm 74.4$  nA·cm<sup>-2</sup>, respectively. Aside from the stable passivation film, the fine microstructures fabricated by laser cladding technique also enable excellent resistance against pitting. Therefore, the LC-built Ti-Nb alloy coatings have good corrosion resistance and could restrain the release of Ni ions.

**Table 3.** Corrosion parameters observed from potentiodynamic polarization for the LC Ti-Nb alloy coatings in the SBF at 37 °C.

Anodes	$E_{corr}$ (vs. SCE)/V	$I_{corr}$ (nA·cm <sup>-2</sup> )	$R_p$ (kΩ·cm <sup>-2</sup> )
c2 coating	$-0.184 \pm 0.005$	$272.4 \pm 15.0$	$218.7 \pm 37.9$
c3 coating	$-0.128 \pm 0.005$	$163.7 \pm 74.4$	$230.2 \pm 18.6$
NiTi alloy	$-0.220 \pm 0.004$	$410.9 \pm 67.7$	$139.6 \pm 3.1$
Laser processed NiTi [59]	-0.200	~500	-
Ti-13Nb-13Zr [56]	-0.556	416.8	-

#### 4. Conclusions

The effects of laser energy density on the microstructures and mechanical properties of the LC-built Ti-Nb coatings were studied. The corrosion resistance of the Ti-Nb coating was also evaluated. The main conclusions of this study can be drawn as following:

1. Ti-Nb coatings with a metallurgical bonding with the NiTi alloy were successfully fabricated by laser cladding. The distribution of the microstructures of the coatings was uniform. The coatings were mainly composed of  $\beta$ -TiNb, NiTi (Nb), and (Ti, Nb)<sub>2</sub>Ni phase. The coatings obtained at lower laser energy density contained a larger proportion of  $\beta$  TiNb and  $\beta$ -Nb phases. The HAZ had large volume of the eutectics consisting of NiTi(Nb) and  $\beta$ -Nb phase with nanometer range crystalline.
2. The size of the grains decreased with energy density, leading to an increase of hardness and elastic modulus. Besides, hardness measurements showed a gradually decreasing trend from the HAZ to the top surface of the coatings, owing to the limited diffusion of Ni atoms from the substrate into the coatings. When the energy density was 88 J·mm<sup>-2</sup>, the microhardness and elastic modulus were  $608 \pm 33.0$  HV and  $111.6 \pm 7.8$  GPa, respectively, which were higher than those of the NiTi alloy (233.1 HV and 54.2 GPa). Besides, the hardness of the HAZ was over 1000 HV. Such high hardness can be associated with the abundant eutectic structure.
3. The LC-built coatings exhibited better corrosion resistance than that of the NiTi alloy, which could effectively ensure the surface qualities and restrain the release of toxic Ni ions. This was attributed to the fine microstructure and to the stable oxide film formed. NiTi alloys with the LC-built Ti-Nb coating are likely to be used as long-time implants.

In the subsequent works, we will continue to regulate a laser scanning strategy to reduce the elastic modulus of the Ti-Nb alloy coatings and investigate the bonding strength between the coatings and substrate.

**Supplementary Materials:** The following are available online at <https://www.mdpi.com/article/10.3390/coatings11050597/s1>, Table S1: Ion concentrations in SBF solution.

**Author Contributions:** J.H. and H.W. contributed to the conception of the study. J.H. contributed significantly to writing the original draft. Y.R., L.L. and J.L. helped perform the analysis with constructive discussions. H.H., Q.H. and R.L. revised the manuscript. All authors have read and agreed to the published version of the manuscript.

**Funding:** This work was supported by the National Natural Science Foundation of China (Grant No. 52071346), the China Postdoctoral Science Foundation (Grant No. 2018M633164). Fundamental Research Funds for the Central Universities of Central South University (Grant No. 2020zzts452).

**Institutional Review Board Statement:** Not applicable.

**Informed Consent Statement:** Not applicable.

**Data Availability Statement:** Not applicable.

**Conflicts of Interest:** The authors declare no conflict of interest.

## References

1. Meisner, S.N.; Yakovlev, E.V.; Semin, V.O.; Meisner, L.L.; Rotshtein, V.P.; Neiman, A.A.; D'yachenko, F. Mechanical behavior of Ti-Ta-based surface alloy fabricated on TiNi SMA by pulsed electron-beam melting of film/substrate system. *Appl. Surf. Sci.* **2018**, *437*, 217–226. [[CrossRef](#)]
2. O'Brien, F.J. Biomaterials & scaffolds for tissue engineering. *Mater. Today* **2011**, *14*, 88–95.
3. Liang, L.X.; Huang, Q.L.; Wu, H.; Ouyang, Z.X.; Liu, T.; He, H.; Xiao, J.; Lei, G.H.; Zhou, K. Stimulation of in vitro and in vivo osteogenesis by Ti-Mg alloys with the sustained-release function of magnesium ions. *Colloid Surf. B Biointerfaces* **2021**, *197*, 111360. [[CrossRef](#)] [[PubMed](#)]
4. Wu, H.; Liang, L.X.; Lan, X.D.; Yin, Y.; Song, M.; Li, R.; Liu, Y.; Yang, H.; Liu, L.; Cai, A.; et al. Tribological and biological behaviors of laser cladded Ti-based metallic glass composite coatings. *Appl. Surf. Sci.* **2020**, *507*, 145104. [[CrossRef](#)]
5. Zheng, L.Z.Y. *Biomedical NiTi Alloy*; Science Publisher: Beijing, China, 2004; pp. 77–95.
6. Xiang, C.; Liu, Y.; Liu, B.; Cao, Y.; Gan, Z. Characterization of hot deformation behavior of Ti-3Al-5Mo-4.5V alloy with a martensitic starting microstructure. *J. Micromech. Mol. Phys.* **2017**, *2*, 1750011. [[CrossRef](#)]
7. Li, H.H.S.; Attallah, M.M.; Adkins, N.J.E.; Ess, K. The development of TiNi-based negative Poisson's ratio structure using selective laser melting. *Acta Mater.* **2016**, *105*, 75–83. [[CrossRef](#)]
8. Bahador, A.; Hamzah, E.; Kondoh, K.; Bakar, T.A.A.; Yusof, F.; Imai, H.; Saud, S.N.; Ibrahim, M.K. Effect of deformation on the microstructure, transformation temperature and superelasticity of Ti-23 at.% Nb shape-memory alloys. *Mater. Des.* **2017**, *118*, 152–162. [[CrossRef](#)]
9. Ahmed, T.; Rack, H.J. Martensitic transformations in Ti-(16–26 at.%) Nb alloys. *J. Mater. Sci.* **1996**, *31*, 4267–4276. [[CrossRef](#)]
10. Kim, H.Y.; Fu, J.; Tobe, H.; Kim, J.I.; Miyazaki, S. Crystal Structure, Transformation Strain, and Superelastic Property of Ti-Nb-Zr and Ti-Nb-Ta Alloys. *Shape Mem. Superelasticity* **2015**, *1*, 107–116. [[CrossRef](#)]
11. Navarro, M.; Michiardi, A.; Castano, O.; Planell, J.A. Biomaterials in orthopaedics. *J. R. Soc. Interf.* **2008**, *5*, 1137–1158. [[CrossRef](#)]
12. Genchi, G.; Carocci, A.; Lauria, G.; Sinicropi, M.S.; Catalano, A. Nickel: Human Health and Environmental Toxicology. *Int. J. Environ. Res. Public Health* **2020**, *17*, 679. [[CrossRef](#)] [[PubMed](#)]
13. Bai, Y.; Deng, Y.; Zheng, Y.; Li, Y.; Zhang, R.; Lv, Y.; Zhao, Q.; Wei, S. Characterization, corrosion behavior, cellular response and in vivo bone tissue compatibility of titanium-niobium alloy with low Young's modulus. *Mater. Sci. Eng. C* **2016**, *59*, 565–576. [[CrossRef](#)]
14. Ureña, J.; Tsipas, S.; Pinto, A.M.; Toptan, F.; Gordo, E.; Jiménez-Morales, A. Corrosion and tribocorrosion behaviour of  $\beta$ -type Ti-Nb and Ti-Mo surfaces designed by diffusion treatments for biomedical applications. *Corros. Sci.* **2018**, *140*, 51–60. [[CrossRef](#)]
15. Shabalovskaya, S.; Andereg, J.; van Humbeeck, J. Critical overview of Nitinol surfaces and their modifications for medical applications. *Acta Biomater.* **2008**, *4*, 447–467. [[CrossRef](#)]
16. Manam, N.S.; Harun, W.S.W.; Shri, D.N.A.; Ghani, S.A.C.; Kurniawan, T.; Ismail, M.H.; Ibrahim, M.H.I. Study of corrosion in biocompatible metals for implants: A review. *J. Alloys Compd.* **2017**, *701*, 698–715. [[CrossRef](#)]
17. Sivakumar, M.; Dhanadurai, K.S.K.; Rajeswari, S.; Thulasiraman, V. Failures in stainless steel orthopaedic implant devices: A survey. *J. Mater. Sci. Lett.* **1995**, *14*, 351–354. [[CrossRef](#)]
18. Wang, L.; Xie, L.; Lv, Y.; Zhang, L.-C.; Chen, L.; Meng, Q.; Qu, J.; Zhang, D.; Lu, W. Microstructure evolution and superelastic behavior in Ti-35Nb-2Ta-3Zr alloy processed by friction stir processing. *Acta Mater.* **2017**, *131*, 499–510. [[CrossRef](#)]
19. Chander, P.; Grzegorz, K.; Sunpreet, S.; Catalin, L.P.; Vinod, M.; Grzegorz, K.; Danil, Y.P.; Alokesh, P. Modification of Ti-6Al-4V alloy by electrical discharge coating process using partially sintered Ti-Nb electrode. *Materials* **2019**, *12*, 1006.
20. Kamachimudali, U.; Sridhar, T.M.; Raj, B. Corrosion of bioimplants. *Sadhana* **2003**, *28*, 601–637. [[CrossRef](#)]
21. Sun, N.X.T.; Liu, C.; Wang, C.; He, J. Bioactive (Si, O, N)/(Ti, O, N)/Ti composite coating on NiTi shape memory alloy for enhanced wear and corrosion performance. *Appl. Surf. Sci.* **2015**, *356*, 599–609. [[CrossRef](#)]
22. Ng, K.W.; Man, H.C.; Yue, T.M. Characterization and corrosion study of NiTi laser surface alloyed with Nb or Co. *Appl. Surf. Sci.* **2011**, *257*, 3269–3274. [[CrossRef](#)]
23. Xiang, K.; Chen, L.-Y.; Chai, L.; Guo, N.; Wang, H. Microstructural characteristics and properties of CoCrFeNiNb<sub>x</sub> high-entropy alloy coatings on pure titanium substrate by pulsed laser cladding. *Appl. Surf. Sci.* **2020**, *517*, 146214. [[CrossRef](#)]
24. Lan, X.; Wu, H.; Liu, Y.; Zhang, W.; Li, R.; Chen, S.; Zai, X.; Hu, T. Microstructures and tribological properties of laser cladded Ti-based metallic glass composite coatings. *Mater. Charact.* **2016**, *120*, 82–89. [[CrossRef](#)]
25. Wu, H.; Liang, L.; Zeng, H.; Lan, X.; Du, J.; Zhou, C.; Liu, Y.; Yang, H.; Li, J.; Cai, A.; et al. Microstructure and nanomechanical properties of Zr-based bulk metallic glass composites fabricated by laser rapid prototyping. *Mater. Sci. Eng. A* **2019**, *765*, 138306. [[CrossRef](#)]
26. Caneda, C.M.; Fogagnolo, J.B.; Kiminami, C.S.; Afonso, C.R.M. Ultrafine eutectic coatings from Fe-Nb-B powder using laser cladding. *Mater. Charact.* **2020**, *160*, 110080. [[CrossRef](#)]

27. Fallah, V.; Corbin, S.F.; Khajepour, A. Process optimization of Ti–Nb alloy coatings on a Ti–6Al–4V plate using a fiber laser and blended elemental powders. *J. Mater. Process. Technol.* **2010**, *210*, 2081–2087. [[CrossRef](#)]
28. Meng, X.L.; Sun, B.; Sun, J.Y.; Gao, Z.Y.; Cai, W.; Zhao, L.C. Microstructure and shape memory behavior of Ti–Nb shape Memory alloy thin film. *Shape Mem. Superelasticity* **2017**, *3*, 230–237. [[CrossRef](#)]
29. Tobe, H.; Kim, H.Y.; Inamura, T.; Hosoda, H.; Nam, T.H.; Miyazaki, S. Effect of Nb content on deformation behavior and shape memory properties of Ti–Nb alloys. *J. Alloys Compd.* **2013**, *577*, S435–S438. [[CrossRef](#)]
30. Kim, H.Y.; Ikehara, Y.; Kim, J.I.; Hosoda, H.; Miyazaki, S. Martensitic transformation, shape memory effect and superelasticity of Ti–Nb binary alloys. *Acta Mater.* **2006**, *54*, 2419–2429. [[CrossRef](#)]
31. Miyazaki, S.; Kim, H.Y.; Hosoda, H. Development and characterization of Ni-free Ti-base shape memory and superelastic alloys. *Mater. Sci. Eng. A* **2006**, *438–440*, 18–24. [[CrossRef](#)]
32. Young, K.H.; Satoru, H.; Il, K.J.; Hosoda, H.; Miyazaki, S. Mechanical properties and shape memory behavior of Ti–Nb alloys. *Mater. Trans.* **2004**, *45*, 2443–2448.
33. Hironobu Matsuno, A.Y.; Watari, F.; Uo, M. Biocompatibility and osteogenesis of refractory metal implants, titanium, hafnium, niobium. *Tantalum Rhenium Biomater.* **2001**, *22*, 1253–1262. [[CrossRef](#)]
34. McMahan, R.E.; Ma, J.; Verkhoturov, S.V.; Munoz-Pinto, D.; Karaman, I.; Rubitschek, F.; Maier, H.J.; Hahn, M.S. A comparative study of the cytotoxicity and corrosion resistance of nickel-titanium and titanium-niobium shape memory alloys. *Acta Biomater.* **2012**, *8*, 2863–2870. [[CrossRef](#)] [[PubMed](#)]
35. Wu, H.; Ren, Y.; Ren, J.; Cai, A.; Baker, I. Effect of melting modes on microstructure and tribological properties of selective laser melted AlSi10Mg alloy. *Virtual Phys. Prototyp.* **2020**, *15*, 570–582. [[CrossRef](#)]
36. Dai, S.L.J.; Zhang, H.; Yu, H.; Chen, C.; Li, Y. Microstructure and high-temperature oxidation resistance of Ti–Al–Nb coatings on a Ti–6Al–4V alloy fabricated by laser surface alloying. *Surf. Coat. Technol.* **2018**, *344*, 479–488. [[CrossRef](#)]
37. Chan, C.-W.; Chang, X.; Bozorgzadeh, M.A.; Smith, G.C.; Lee, S. A single parameter approach to enhance the microstructural and mechanical properties of beta Ti–Nb alloy via open-air fiber laser nitriding. *Surf. Coat. Technol.* **2020**, *383*, 125269. [[CrossRef](#)]
38. Fallah, V.; Corbin, S.F.; Khajepour, A. Solidification behaviour and phase formation during pre-placed laser cladding of Ti45Nb on mild steel. *Surf. Coat. Technol.* **2010**, *204*, 2400–2409. [[CrossRef](#)]
39. Liu, S.; Liu, J.; Wang, L.; Ma, R.L.-W.; Zhong, Y.; Lu, W.; Zhang, L.-C. Superelastic behavior of in-situ eutectic-reaction manufactured high strength 3D porous NiTi–Nb scaffold. *Scr. Mater.* **2020**, *181*, 121–126. [[CrossRef](#)]
40. Wang, M.J.M.; Liao, G.; Guo, X.Z.S. Martensitic transformation involved mechanical behaviors and wide hysteresis of NiTiNb shape memory alloys. *Prog. Nat. Sci. Mater. Int.* **2012**, *22*, 130–138. [[CrossRef](#)]
41. Liu, S.; Han, S.; Zhang, L.; Chen, L.-Y.; Wang, L.; Zhang, L.; Tang, Y.; Liu, J.; Tang, H.; Zhang, L.-C. Strengthening mechanism and micropillar analysis of high-strength NiTi–Nb eutectic-type alloy prepared by laser powder bed fusion. *Compos. Part B Eng.* **2020**, *200*, 108358. [[CrossRef](#)]
42. Fan, Y.; Jin, G.; Cui, X.; Li, Y.; Gao, Z. Effect of Nb and CeO<sub>2</sub> on the mechanical and tribology properties of Co-based cladding coatings. *Surf. Coat. Technol.* **2016**, *288*, 25–29. [[CrossRef](#)]
43. Ren, Y.; Liang, L.; Shan, Q.; Cai, A.; Wu, H. Effect of volumetric energy density on microstructure and tribological properties of FeCoNiCuAl high-entropy alloy produced by laser powder bed fusion. *Virtual Phys. Prototyp.* **2020**, *15* (Suppl. 1), 543–554. [[CrossRef](#)]
44. Wu, H.; Ren, J.Y.; Huang, Q.L.; Zai, X.; Li, R. Effect of laser parameters on microstructure, metallurgical defects and property of AlSi10Mg printed by selective laser melting. *J. Micromech. Mol. Phys.* **2017**, *2*, 1750017. [[CrossRef](#)]
45. Chakraborty, R.; Datta, S.; Raza, M.S.; Saha, P. A comparative study of surface characterization and corrosion performance properties of laser surface modified biomedical grade nitinol. *Appl. Surf. Sci.* **2019**, *469*, 753–763. [[CrossRef](#)]
46. Surmeneva, M.A.; Koptyug, A.; Khrapov, D.; Ivanov, Y.F.; Mishurova, T.; Evsevlev, S.; Prymak, O.; Loza, K.; Epple, M.; Bruno, G.; et al. In situ synthesis of a binary Ti–10 at.% Nb alloy by electron beam melting using a mixture of elemental niobium and titanium powders. *J. Mater. Process. Technol.* **2020**, *282*, 116646. [[CrossRef](#)]
47. Zhao, X.; Yan, X.; Yang, Y.; Xu, H. Wide hysteresis NiTi(Nb) shape memory alloys with low Nb content (4.5 at.%). *Mater. Sci. Eng. A* **2006**, *438*, 575–578. [[CrossRef](#)]
48. Schütze, M. Metallic and ceramic coatings: Production, high temperature properties and applications. In *Materials and Corrosion*; Vasantasree, V., Hocking, M.G., Sidky, P.S., Eds.; Longman Scientific & Technical Ltd.: Harlow, UK, 1989.
49. Zhang, H.L.Y.; Jin, Z. Thermodynamic assessment of the Nb–Ti system. *Calphad* **2001**, *25*, 305–317. [[CrossRef](#)]
50. Elahinia, M.; Moghaddam, N.S.; Andani, M.T.; Amerinatanzi, A.; Bimber, B.A.; Hamilton, R.F. Fabrication of NiTi through additive manufacturing: A review. *Prog. Mater. Sci.* **2016**, *83*, 630–663. [[CrossRef](#)]
51. Mulliken, R.S. Electronic population analysis on LCAO–MO molecular wave functions 1, 2, 3, 4. *J. Chem. Phys.* **1955**, *23*, 1833–1840. [[CrossRef](#)]
52. Masahiko, M. ; *A Quantum Approach to Alloy Design*; Elsevier: Amsterdam, The Netherlands, 2019; pp. 77–94.
53. Shiva, S.; Palani, I.A.; Mishra, S.K.; Paul, C.P.; Kukreja, L.M. Investigations on the influence of composition in the development of Ni–Ti shape memory alloy using laser based additive manufacturing. *Opt. Laser Technol.* **2015**, *69*, 44–51. [[CrossRef](#)]
54. Zhao, D.; Han, C.; Li, J.; Liu, J.; Wei, Q. In situ fabrication of a titanium-niobium alloy with tailored microstructures, enhanced mechanical properties and biocompatibility by using selective laser melting. *Mater. Sci. Eng. C* **2020**, *111*, 110784. [[CrossRef](#)]

55. Wang, Q.; Han, C.; Choma, T.; Wei, Q.; Yan, C.; Song, B.; Shi, Y. Effect of Nb content on microstructure, property and in vitro apatite-forming capability of Ti-Nb alloys fabricated via selective laser melting. *Mater. Des.* **2017**, *126*, 268–277. [[CrossRef](#)]
56. Zhou, L.; Yuan, T.; Tang, J.; He, J.; Li, R. Mechanical and corrosion behavior of titanium alloys additively manufactured by selective laser melting—A comparison between nearly  $\beta$  titanium,  $\alpha$  titanium and  $\alpha + \beta$  titanium. *Opt. Laser Technol.* **2019**, *119*, 105625. [[CrossRef](#)]
57. Chui, P.; Jing, R.; Zhang, F.; Li, J.; Feng, T. Mechanical properties and corrosion behavior of  $\beta$ -type Ti-Zr-Nb-Mo alloys for biomedical application. *J. Alloys Compd.* **2020**, *842*, 155693. [[CrossRef](#)]
58. Shi, Z.; Liu, M.; Atrens, A. Measurement of the corrosion rate of magnesium alloys using Tafel extrapolation. *Corros. Sci.* **2010**, *52*, 579–588. [[CrossRef](#)]
59. Marattukalam, J.J.; Singh, A.K.; Datta, S.; Das, M.; Balla, V.K.; Bontha, S.; Kalpathy, S.K. Microstructure and corrosion behavior of laser processed NiTi alloy. *Mater. Sci. Eng. C* **2015**, *57*, 309–313. [[CrossRef](#)]